Applied Acoustics 203 (2023) 109166

Contents lists available at ScienceDirect

Applied Acoustics

journal homepage: www.elsevier.com/locate/apacoust

# An ultra-thin low-frequency broadband metasurface with near-zero suppression of aerodynamic acoustic pressure

Min Li [a,b], Jiuhui Wu [a,b,*], Bobo Wu [c], Fuyin Ma [a,b], Chongrui Liu [a,b], Xiaoyang Yuan [a], Yangbin Sun [d]

[a] School of Mechanical Engineering, Xi'an Jiaotong University, Xi'an 710049, China
[b] State Key Laboratory for Strength and Vibration of Mechanical Structures, Xi'an Jiaotong University, Xi'an 710049, China
[c] Qingdao Laboratory, Institute of Acoustics, Chinese Academy of Sciences, Qingdao 266109, China
[d] National Key Laboratory on Ship Vibration and Noise, China Ship Development and Design Center, Wuhan 430064, China

ARTICLE INFO

*Article history:*
Received 26 December 2021
Received in revised form 30 October 2022
Accepted 6 December 2022

*Keywords:*
Low-frequency broadband acoustic metasurface
Near-zero suppression of low-frequency aerodynamic acoustic pressure
Lotus-pods-neck Helmholtz resonator
1/4-scale Ahmed body
Wind tunnel test

ABSTRACT

A near-zero suppression mechanism of aerodynamic acoustic pressure is revealed by adopting the ultra-thin low-frequency broadband lotus-pods-neck Helmholtz resonator (LPNHR) metasurface presented in this paper. The LPNHR is designed by changing the single neck of a Helmholtz resonator (HR) to a lotus-pods multi-layer-hole neck and keeping the number and equivalent diameter of the holes in the upper layer greater than that in the lower layer, and the bandwidth of LPNHR could be much widened than that of HR since the reduced acoustic mass. During the incident fluid flow, compared with HR, greater pressure difference formed at the interface of each hole of LPNHR generates stronger multi-vortexes inside its neck. Larger multi-vortex areas with greater absorption area ratio significantly increase the average flow velocity at the neck interface of LPNHR, resulting in decreased impedance. Moreover, the stronger multi-vortexes weaken the influence of the main-flow on the fluid flow inside the neck, that is, the flow from the external flow field into the LPNHR neck is enhanced under the action of the strong vortexes. The impedance decreases further and the effective length of the neck and acoustic mass increase, the shift of the flow-influenced sound attenuation to higher frequencies is suppressed and turned to lower frequencies. When the impedance approaches zero, the incident and scattered acoustic pressure match in phase and the acoustic pressure fluctuation at the wall will be fundamentally suppressed. Which is the physical mechanism of LPNHR to achieve near-zero suppression of low-frequency aerodynamic acoustic pressure. Furthermore, by adjusting the multiple parameters of LPNHR, the near-zero suppression of lower-frequency and larger-bandwidth aerodynamic acoustic pressure at higher speed could be achieved. Finally, an average reduction of sound pressure level by 3.71 dB (A) in the range of 550 Hz–4150 Hz on the 1/4-scale Ahmed body surface at a speed of 50 m/s is experimentally verified through 26 mm thick LPNHR metasurface with a basic unit composed of six parallel cells. The near-zero aerodynamic acoustic pressure suppression mechanism with metasurface presented provides new approaches for low frequency aerodynamic noise control, showing great potential in engineering applications.



## 1. Introduction

With the continuous increase in operating speed, the dynamic environment of the ground traffic has undergone qualitative changes from the basis of the mechanical and electrical to that dominated by aerodynamics [1]. The flow separation occurs at the irregular surface forming complex vortexes as the object in motion interacts with the air, which generates large fluctuating pressure and in turn induces great aerodynamic noise [2–4]. Aerodynamic noise has become the main source of high-speed traffic noise and the decisive factor to limit the further increase of the speed [5]. The dipole noise is regarded as the main noise source of the vehicle body and is usually described by the fluctuating pressure on the body surface [2,6]. Obviously, suppressing the fluctuating pressure around the skin surface is the basis for controlling the aerodynamic noise. Driven by the rapid development of high-speed transportation, remarkable achievements have been made in the aerodynamics research. Numerous studies have shown that the energy distribution of the aerodynamic noise on the vehicle surface presents low-frequency and broadband characteristics with no obvious main frequencies [3,4,7]. Acoustic metamaterials with excellent low-frequency performance have developed rapidly

* Corresponding author at: School of Mechanical Engineering, Xi'an Jiaotong University, Xi'an 710049, China.
*E-mail address:* ejhwu@mail.xjtu.edu.cn (J. Wu).

https://doi.org/10.1016/j.apacoust.2022.109166
0003-682X/

in recent years and are usually designed to match the acoustic impedance of the background medium to maximize the absorption effect [8–12]. However, for the boundary conditions under incident fluid flow [13–15], the acoustic impedance at the wall depends not only on the characteristics of the wall material, but is more affected by the characteristics of the mean flow and parameters of the flow disturbance. Radavich et al. simulated the complex interaction between the fluid flow and acoustic resonance at low Mach numbers with the solution of the unsteady, turbulent and compressible Navier-Stokes equations, which reproduced the physical process of flow-acoustic coupling and predicted the coupled flow-acoustic problems for a system with two coaxial side branches [16]. Aiming at the problem that the acoustic performance of the muffler element decreases with the increase of the exhaust gas flow, Howard et al. tested the effect of fluid flow on the acoustic attenuation of side branches with different geometries on an adaptive quarter-wave tube and found that the side-branch with a bell-mouth geometry resulted in greatest noise reduction due to the smallest acoustic impedance and least affection by airflow [17]. Philips and Hersh observed in their experimental study that the acoustic resistance increased linearly with the increase of the mean flow velocity, which also explained the reduction in transmission loss caused by the introduction of the mean flow [18,19]. Meyer et al. studied the effect of the turbulent airflow on the sound attenuation of different sound-absorbing materials through experiments and found that the maximum attenuation value decreased with increasing flow velocity and shifted to higher frequencies [20]. Anderson also found that the basic resonant frequency of the resonator increased with the increase of the flow velocity by testing a single-sided branch Helmholtz resonator in a circular pipe [21]. David et al. investigated the acoustic properties and flow laws in rectangular lined channels with grazing jets and found that the acoustic transmission coefficient was the smallest at the resonant frequency of the resonator in the absence of fluid flow, while the sound transmission near the resonance frequency increased strongly with the increase of the Mach number of the grazing flow [22]. Thus, under the weakening of the flow field on the sound attenuation, the specific acoustic impedance of the structure no longer matches that of the medium. According to the definition, when the impedance at the boundary is close to zero, the pressure perturbation in the flow field will no longer be excited and the acoustic pressure could be fundamentally suppressed. In the study of controlling the hypersonic boundary layer with metasurfaces, Zhao et al. proved that the out-of-phase behavior of the incident and reflected wave at the resonance frequency minimized the near-wall acoustic pressure when the boundary impedance changed from infinity to nearly zero, which largely inhibited the growth of Mack's second mode [23].

Traditional HRs have a wide range of applications in the low-frequency sound absorption and noise reduction, while the shortcomings of narrow sound absorption band restrict its performance [24–26]. Although the transition from the single-hole HR to micro-perforated structure could reduce the acoustic mass and obtain broadband control [27–29], it is not conducive to low-frequency absorption. Whether it is HR or micro-perforated structure, the low-frequency and broadband control are often contradictory. Inspired by this, we present a near-zero suppression mechanism of low-frequency broadband aerodynamic acoustic pressure with a novel acoustic metasurface by changing the single neck of HR to a lotus-pods multi-layer-hole neck with greater number and equivalent diameter of holes in upper layer than that in lower layer. When the number of holes in the lower layer is equal to that in the upper layer, the structure is equivalent to the parallel connection of micro-perforated HRs, and while the number of the holes in the upper layer is equal to that in the lower layer and is 1, the structure degrades to the parallel connection of HRs. The bandwidth of LPNHR could be broadened than HR due to the decrease of the acoustic mass of the multi-holes in the upper layers, and low-frequency control could be achieved together by adjusting the parameters of the holes in the lower layers. The near-zero suppression mechanism of low-frequency aerodynamic acoustic pressure under the action of incident flow is investigated, and acoustic metasurfaces are designed to achieve effective reduction of the low-frequency and broadband aerodynamic noise at a speed of 50 m/s.

This paper is organized as follows: in Section 2, the physical model of the proposed metasurface is first introduced. The acoustic impedance of LPNHR is then theoretically derived by using the plane wave expansion method and broadband suppression mechanism of LPNHR is investigated; in Section 3, the fluid-acoustic coupling simulation model of the 1/4-scale Ahmed body at different speed is established and low-frequency aerodynamic acoustic pressure suppression mechanism of LPNHR is then analyzed. Moreover, the investigations of the effects that the key parameters and main-flow velocities on suppressing aerodynamic acoustic pressure are carried out; in Section 4, a ultra-thin LPNHR metasurface with low-frequency and broadband suppression for aerodynamic noise at a speed of 50 m/s is realized, and the noise reduction effect is detected by the wind tunnel test. Finally, several conclusions are drawn in Section 5.

## 2. Broadband suppression mechanism of LPNHR

### 2.1. Structure of the LPNHR cell

The proposed LPNHR is established by changing the neck of HR to a lotus-pods multi-layer-hole neck without changing other dimensions, which consists of a rectangular cavity and a lotus-pods neck. As shown in Fig. 1(a)-(c), the length, width and height of the rectangular cavity $i$ is respectively $2a_i$, $2b_i$ and $H_i$, $i$ = 1, 2, 3...$N$-1, $N$. The lotus-pods neck is composed of different numbers of cylindrical holes connected by thin cavities, that is, the first-layer holes $i$ with a diameter of $d_i$ and a length of $h_i$ are connected by a thin cavity $ii$ with a height of $H_{ii}$ to the second-layer holes $ii$ with a diameter and length of $d_{ii}$ and $h_{ii}$, and so on. The number and equivalent diameter of the cylindrical holes increase layer by layer from bottom to top for a lotus-shaped distribution, that is, $n_{ii} > n_i \geq 1$ and $n_{ii}d_{ii} > n_i d_i$, and the length and width of the thin cavity $ii$ are consistent with the rectangular cavity $i$. The corresponding cell periods are $l_i$ and $w_i$, and the absorption area ratio is defined as $\varphi_i = n_{ii}\pi {d_{ii}}^2/(4S_i)$, and the incident area of the cell is $S_i = l_i w_i$. For better comparative study, the height of HR neck is $h_0 = h_i + H_{ii} + h_{ii}$. We start by presenting the suppression mechanism of aerodynamic acoustic pressure of the second-order LPNHR with geometrical parameters of $2a_1$ = 7 mm, $n_{11}$ = 5, $2b_1 = 2a_1/n_{11}$ = 1.4 mm, $H_1$ = 22 mm, $l_1$ = 7.5 mm, $w_1$ = 1.9 mm, $n_1$ = 1, $d_1$ = 0.9 mm, $h_1$ = 5 mm, $H_{11}$ = 0.5 mm, $d_{11}$ = 1.2 mm and $h_{11}$ = 4 mm.

### 2.2. Theoretical calculation of the acoustic impedance

The plane wave transfer matrix method is first used to derive the specific acoustic impedance of the second-order LPNHR, the acoustic pressure $P_{nii}$ and the mass velocity $v_{nii}$ at the interface of the hole $ii$ [30] can be written as

$$\begin{bmatrix} P_{nii} \\ v_{nii} \end{bmatrix} = \mathrm{T_{nii}}\mathrm{T_{cii}}\mathrm{T_{ni}} \begin{bmatrix} P_{ci} \\ v_{ci} \end{bmatrix} \tag{1}$$

where $\mathrm{T_{nii}}$, $\mathrm{T_{cii}}$ and $\mathrm{T_{ni}}$ are the impedance transfer matrix of the hole $ii$, cavity $ii$ and hole $i$, respectively, and $\mathrm{T_{nii}} = \begin{bmatrix} 1 & Z_{nii} \\ 0 & 1 \end{bmatrix}$,

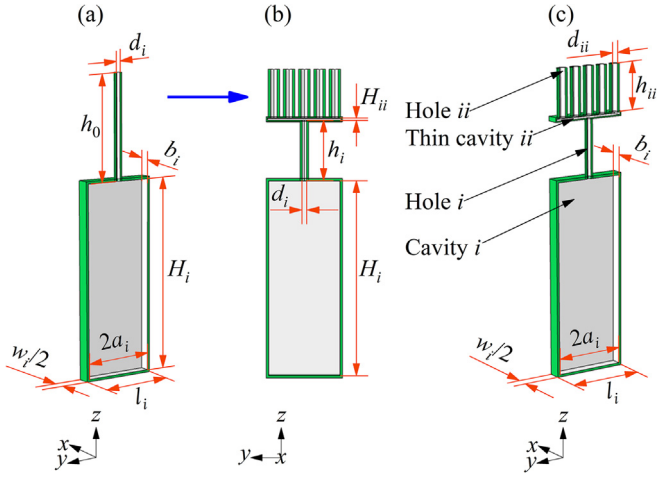


**Fig. 1.** (a) 3D Schematic view of HR, (b) Cross section of LPNHR in the *y*-*z* plane and (c) 3D Schematic view of LPNHR.

$T_{cii} = \begin{bmatrix} 1 & jZ_{cii}\tan k_{cii}H_{ii} \\ (j\tan k_{cii}H_{ii})/Z_{cii} & 1 \end{bmatrix}$, $T_{ni} = \begin{bmatrix} 1 & Z_{ni} \\ 0 & 1 \end{bmatrix}$, $P_{ci}$ and $v_{ci}$ are the acoustic pressure and mass velocity on the interface of cavity *i*.

The specific impedances $Z_{ni}$ and $Z_{nii}$ of the cylindrical hole *i* and hole *ii* [31] are given by

$$Z_{nx} = \frac{j\omega\rho_\omega h_x}{\varphi_x}\left[1 - \frac{2B_1\left(\chi_x\sqrt{-j}\right)}{\left(\chi_x\sqrt{-j}\right)B_0\left(\chi_x\sqrt{-j}\right)}\right]^{-1} + \frac{\sqrt{2}\mu\chi_x}{d_x\varphi_x} + j\frac{0.85\omega\rho_\omega d_x}{\varphi_x},\ x = i, ii \tag{2}$$

where $\rho_\omega$ and $c_\omega$ are density of the air medium and speed of sound, respectively, $\chi_x = d_x\sqrt{\frac{\omega\rho_\omega}{4\mu}}$, $x = i, ii$, is the perforation constant of the neck, dynamic viscosity is $\mu$=1.8 × $10^{-5}$ Pa·s, $B_0$ and $B_1$ are the zeroth and first order Bessel function of first kind, respectively. The specific impedance of the thin cavity *ii* can be expressed as $Z_{cii}$= $\sqrt{\rho_{cii}/C_{cii}}$ according to the thermo-viscous acoustic theory, and $\rho_{cii}$ and $C_{cii}$ are the dynamic density and compressibility [32].

Assuming that any plane wave is incident on the surface of the structure along the negative direction of the *z* axis and decomposed into the incident plane wave and the scattered sound wave. The periodicities $l_i$ and $w_i$ are much smaller than the acoustic wavelength, and the interface of the cavity *i* is at *z* = 0. The specific impedance $Z_{ci}$ of the cavity *i* and the normalized effective surface acoustic impedance $Z_i$ of the second-order LPNHR can be expressed as

$$Z_{ci} = \frac{1}{\rho_\omega c_\omega}\frac{P_{ci}}{v_{ci}}|_{z=0} = 1 + \frac{1}{j\tan(k_{ci}H_i)\frac{4a_ib_i}{l_iw_i}\left(\frac{\rho_\omega}{\rho_{ci}}\right)\left(\frac{k_{ci}}{k_0}\right)} - \sum_{r,s=-\infty}^{r,s=+\infty}\frac{k_0}{\sqrt{k_0^2 - \left(\frac{2\pi r}{l_i}\right)^2 - \left(\frac{2\pi s}{w_i}\right)^2}}S_{rs}^2 \tag{3}$$

$$Z_i = \frac{1}{\rho_\omega c_\omega}\frac{P_{nii}}{v_{nii}}|_{z=h_i+H_{ii}+h_{ii}} = Z_{ci} + Z_{ni} + Z_{cii} + Z_{nii} \tag{4}$$

where $\rho_{ci}$ is the dynamic density [13,33], $k_{ci}$ and $k_0 = \omega/c_\omega$ are the wavenumber inside the cavity and at the wall. $S_{rs} = \mathrm{sinc}\left(k_x^{(r)}a_i\right)\mathrm{sinc}\left(k_y^{(s)}b_i\right)$ is the overlap integral among the *r*th-order and *s*th-order diffracted mode and fundamental mode inside the cavity, $k_x^{(r)} = k_x + 2\pi r/l_i$, $k_y^{(s)} = k_y + 2\pi s/w_i$.

Based on the definition of the boundary conditions at the wall, the specific impedance with fluid flow can be expressed as $Z_i = (P_i + P_s)/v_z$, in which $P_i$ and $P_s$ are the incident acoustic pressure and scattered acoustic pressure including fluctuating acoustic pressure at the wall, and $v_z$ is the normal flow velocity. The acoustic pressure fluctuation cannot be effectively suppressed through impedance matching because of the continuous supply of energy to the boundary layer by the flow field [23]. When the impedance $Z_i$ is equal to zero, the total acoustic pressure $P_i$ + $P_s$ at the wall could be theoretically equal to zero, which means that the incident and scattered sound wave match in phase and the acoustic pressure fluctuation at the wall will be fundamentally suppressed, thus the aerodynamic noise could be minimized. Despite the consensus of the non-zero impedance under the influence of the inherent viscous heat losses, the study of near-zero acoustic pressure suppression is of great significance for the aerodynamic noise reduction.

### 2.3. Broadband suppression of LPNHR with no fluid flow

Fig. 2 compares the surface average acoustic impedance of HR and LPNHR, the simulation results are basically consistent with the theoretical analysis. The results show that the impedance peak of HR at 890 Hz is close to 0.111, while the impedance peak of LPNHR at 1110 Hz is about 0.141. Although the peak shifts from 890 Hz to 1110 Hz, the bandwidth corresponding to LPNHR increases by 56.6 % from 106 Hz of HR to 166 Hz when the impedance is 0.5. The broadband control mechanism of LPNHR can be explained based on the relationship between the bandwidth $\Delta f_i$ and the quality factor $Q_i$ of the resonance system, the quality factor meets $1/Q_i = \Delta f_i/f_i$ and $Q_i = \omega m_i/r_i$, the resonance frequency is $f_i = 1/2\pi\sqrt{k_i/m_i}$, $k_i$ is the equivalent stiffness, which is $k_i = c_\omega{}^2/V_{ci}$ for the first-order system and $k_i = k_{ci} + k_{cii} = c_\omega{}^2/V_{ci} + c_\omega{}^2/V_{cii}$ for the second-order system. Then the bandwidth can be simplified as $\Delta f_i = r_i/2\pi m_i$, and $m_i$ and $r_i$ are the acoustic mass and relative specific resistance of the structure. The relative specific impedance of LPNHR calculated by electric-acoustic analogy can be written as

$$Z_i = r_i + j(\omega m_i - 1/\omega c_i) \tag{5}$$

$$r_i = r_{ni} + r_{nii} + r_{ci} + r_{cii} \tag{6}$$

$$r_{nx} = \frac{32\mu h_x}{\rho_\omega c_\omega \varphi_x d_x{}^2}\left(\sqrt{1 + \frac{\chi_x{}^2}{32}} + \frac{\sqrt{2}}{32}\frac{\chi_x d_x}{h_x}\right),\ x = i, ii \tag{7}$$

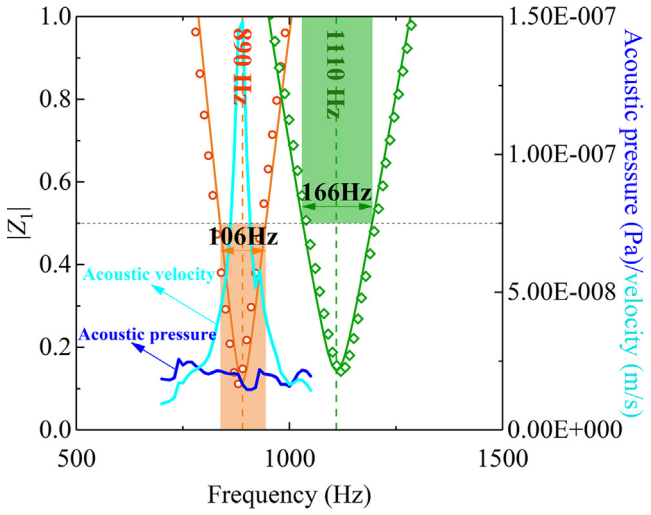


**Fig. 2.** Comparison of the acoustic performance of HR and LPNHR when there is no fluid flow.

$$r_{cx} = R_e\left(\frac{Z_{cx}}{\rho_\omega c_\omega}\right),\ x = i,\ ii \tag{8}$$

$$m_i = m_{ni} + m_{nii} + m_{ci} + m_{cii} \tag{9}$$

$$m_{nx} = \frac{h_x}{c_\omega \varphi_x}\left(1 + \frac{1}{\sqrt{9+\chi_x{}^2/2}} + 0.85\frac{d_x}{h_x}\right),\ x = i,\ ii \tag{10}$$

$$m_{cx} = \rho_\omega V_{cx}/3S_{cx}{}^2,\ x = i,\ ii \tag{11}$$

$$c_i = c_{ci} + c_{cii} \tag{12}$$

$$c_{cx} = V_{cx}/\rho_\omega c_\omega{}^2,\ x = i,\ ii, \tag{13}$$

where $j(\omega m_i - 1/\omega c_i)$ is the relative specific reactance, $c_i$ represents the relative specific capacitance, $r_{ni}$, $r_{nii}$, $r_{ci}$ and $r_{cii}$ are the resistance of the hole *i*, hole *ii*, cavity *i* and thin cavity *ii*, $m_{ni}$, $m_{nii}$, $m_{ci}$ and $m_{cii}$ are the acoustic mass of the hole *i*, hole *ii*, cavity *i* and thin cavity *ii*, respectively, $V_{ci}$ and $V_{cii}$ are the volume of cavity *i* and thin cavity *ii*, $S_{ci}$ and $S_{cii}$ are the cross-sectional area of the cavity *i* and thin cavity *ii*.

$Z_i$ and $Z_{HR}$ at the resonance frequency are both pure and real numbers and close to zero, that is, $r_i > r_{HR} \approx 0$. Under the condition of keeping other parameters unchanged, the improvement from a single neck to a lotus-pods neck with the same length makes the acoustic mass satisfy $m_i < m_{HR}$, therefore, there is $\Delta f_i > \Delta f_{HR}$, LPNHR has more advantages in realizing broadband control compared with HR without introducing more detuned cells.

## 3. Low-frequency aerodynamic acoustic pressure suppression mechanism of LPNHR with incident fluid flow

### 3.1. Simulation modeling

A flow-acoustics coupling simulation modeling of the 1/4-scale Ahmed body at different speed is conducted by using the commercial finite element software COMSOL Multiphysics™ 5.4 based on the computational fluid dynamics (CFD) and acoustics to predict the distribution of the aerodynamic noise on the Ahmed body surface and explore the physical mechanism of LPNHR for the aerodynamic noise reduction. As shown in Fig. 3 (a), a *k*-ε turbulence computational model is established first to analyze the flow field characteristics around the Ahmed body and the wall function is used to describe the near-wall region. The 1/4-scale Ahmed body with length ($L$) of 261 mm, and width ($W$) of 84.5 mm and height ($H$) of 97.25 mm is placed in the computational domain with length, width and height of 8$L$, 2$L$ and 2$L$, respectively. Four cylindrical legs of 7.5 mm in diameter are attached to the Ahmed bottom surface, and the LPNHR is designed along the longitudinal centerline on the Ahmed upper surface. The rear slant angle of the Ahmed body is 25°, and the front end of the Ahmed body is 2$L$ from the flow inlet surface of the computational domain [34]. Air enters the computational domain at a speed of $U_0$ = 50 m/s perpendicular to the inlet surface, and the Reynolds number based on the length ($L$) and the flow velocity ($U_0$) is 8.93 × $10^5$. The front face of the computational domain is set as velocity inlet boundaryand the rear face is set as pressure outlet boundary. The surface of the Ahmed body and the lower surface of the computational domain are set as wall functions and no-slip boundaries, and the remaining surfaces of the computational domain are set as slip boundaries. The surface of the Ahmed body is meshed by triangular and quadrilateral elements, and the meshing of the computational domain is mainly tetrahedrons. Six boundary-layer meshes with a ratio of 1:1.2 are set near the wall, and the thickness of the first boundary layer is 0.2 mm. Mesh control entities are added behind the Ahmed body to more accurately analyze the wake and will be removed after the complete meshing. The total number of the computational meshes of the CFD model is 1072763.

Since the CFD analysis requires fine meshing and the acoustic meshing has no significant effect on the results of acoustic analysis, then the CFD and acoustic models are solved with the different meshes. By solving the CFD model, the turbulent variables such as pressure $P_0$, velocity $U_0$ and dynamic viscosity $\mu_0$ could be obtained. Then, the flow field variables $P_0$, $U_0$ and $\mu_0$ are mapped respectively to the corresponding variables $P_{aco}$, $U_{aco}$, and $\mu_{ac0}$ in the acoustic field by solving the weak form of the partial differential equations [32]. Finally, the mapped variables $P_{aco}$, $U_{aco}$, and $\mu_{ac0}$ are input into the acoustic model to solve the acoustic problem,

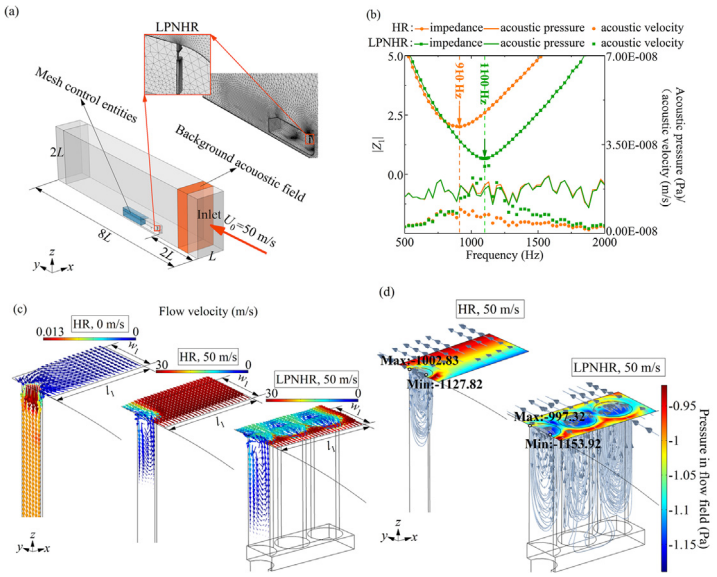


**Fig. 3.** (a) Simulation modeling and meshing of the 1/4-scale Ahmed body with LPNHR on the upper surface. (b) Comparison of the acoustic performance of HR and LPNHR at a speed of 50 m/s. (c) The velocity vector arrow of HR and LPNHR when $U_0$ is 0 m/s and 50 m/s. The arrows indicate the direction of the fluid flow and the color represents the magnitude of flow velocity. (d) Distribution of the pressure and streamline around the neck of HR and LPNHR with a flow velocity of 50 m/s.

thus the coupling of the flow field and the sound field is realized. The flow-acoustic coupling modeling has been fully verified in previous works [32,34], which can realize the accurate prediction and analysis of aerodynamic noise. Acoustics is solved by the Naiver-Stokes equations, the background plane sound wave is introduced downstream of the system (along the $y$ axis) with average flow velocity of $U_0$ = 50 m/s and added as a background acoustic field feature to a smaller orange region as shown in Fig. 3(a), and the background acoustic pressure $P_b$, wave number $k_0$, background velocity $U_b$ and background temperature $T_b$ are respectively defined as $P_b = P_0 \cdot e^{-ik_0 y}$, $P_0 = 1\ Pa$, $k_0 = \frac{\omega}{c_\omega + U_0}$, $U_b = -\frac{1}{i\omega\rho_\omega} \cdot \frac{\partial P_b}{\partial y}$ and $T_b = \frac{\chi_p T_0}{\rho_\omega c_p} P_b$ [32].

### 3.2. Low-frequency aerodynamic acoustic pressure suppression mechanism

Compared with the acoustic performance of LPNHR and HR in Fig. 2 and Fig. 3(b), the impedance peak of HR increases from 0.111 to 2 and the frequency of the peak shifts from 890 Hz to a higher frequency of 910 Hz as $U_0$ increases from 0 m/s to 50 m/s, and the impedance peak of LPNHR increases from 0.141 to 0.663 and the frequeny of the peak shifts from 1110 Hz to a lower frequency of 1100 Hz as $U_0$ increases from 0 m/s to 50 m/s. Little change in acoustic pressure and significant decrease in normal acoustic velocity of HR at the impedance peak are the direct cause of the rapid increase in impedance when $U_0$ increases from 0 m/s to 50 m/s. The acoustic velocity corresponding to the impedance peak of LPNHR with $U_0$ of 50 m/s is significantly larger than that of HR, which explains well that the peak impedance of LPNHR at the same speed is much smaller than HR as the acoustic pressure is not much different.

Fig. 3(c) shows the flow field characteristics in and around HR and LPNHR within a cell period when $U_0$ is 0 m/s and 50 m/s, the color describes the magnitude of the flow velocity and the arrows show the direction of the fluid flow. Fig. 3(d) shows the distribution of the pressure inside HR and LPNHR under the main flow of $U_0$ = 50 m/s, and both the maximum and minimum pressures appear on the HR and LPNHR interfaces. When $U_0$ is 0 m/s, the external main-flow field is largely affected by the fluid flow inside the neck of HR and a large amount of external fluid flows toward the inlet of the neck, so that the effective length of the neck is greater than its geometric length [35,36]. In this case, the occurrence of resonance inside the HR neck reaches the largest energy dissipation, the acoustic velocity at the neck interface is much greater than the acoustic pressure (as shown in Fig. 2) and the impedance is close to zero. However, when $U_0$ is 50 m/s, a maximum pressure difference of 125 Pa generated at the HR interface produces a counterclockwise shear force, thus forming counterclockwise vortexes inside the HR neck and causing a slip velocity at the neck interface consistent with the direction of the main flow. The interaction between the neck and the main flow is obviously weakened, resulting in significantly decreased normal acoustic velocity at the HR interface and much increased impedance in Fig. 3(b) compared to Fig. 2. The weakening of the external fluid flow into the neck causes the decrease of effective length of the HR neck and thereby the decrease of the acoustic mass, which is the main reason that the impedance peak of HR moves to higher frequencies with the increasing main flow and consistent with the previous researches by Selamet and Anderson et al. on the sound attenuation of HR influenced by the fluid flow [21,37]. When the main flow with same velocity flows through the LPNHR interface, a larger pressure difference of 156.6 Pa generates at the interface of any one hole 11 and stronger multi-vortexes are formed inside the LPNHR neck. On the one hand, greater multi-vortex areas with larger absorption area ratio significantly increase the average flow velocity at the LPNHR interface according to the theory of the central vortex that the flow velocities of the vortex lines are proportional to the distance from the center point [38], then the acoustic impedance decreases. On the other hand, stronger multi-vortexes weaken the influence of the main flow on the fluid flow inside the neck, while the flow from the external flow field into the LPNHR neck is enhanced under the action of the strong vortexes. The impedance decreases further and the effective length of the neck and acoustic mass increase, the shift of impedance peak to higher frequency due to the decreased acoustic mass affected by the increased main-flow velocity is suppressed and turned to lower frequency. When the impedance is equal to zero, the amplitude of the incident and scattered acoustic pressure at the LPNHR interface are equal and the phase of them are opposite, the total acoustic pressure could be effectively suppressed so as to control the excitation of the dipole source aerodynamic noise caused by the pressure fluctuation in the flow field. It can be concluded that LPNHR could reduce the impact of the increasing flow on the acoustic impedance and resist the sound attenuation from shifting to higher frequency, which is the physical mechanism of LPNHR to realize near-zero suppression of low-frequency aerodynamic acoustic pressure.

### 3.3. Effects of parameters and main-flow velocities on the acoustic pressure suppression

#### 3.3.1. Parameters of neck with different main-flow velocities

In Fig. 4(a) and (b), the effects of the number and diameter of hole11 with different main-flow velocities on the acoustic performance of LPNHR are investigated in details. When $U_0$ is 0 m/s, it can be found that the magnitude of the impedance peak decreases from 0.15 to 0.141 when the number $n_{11}$ of hole11 increases from 1 to 5 and from 0.21 to 0.141 as the diameter $d_{11}$ of hole11 increases from 0.5 mm to 1.2 mm, and the frequency of the impedance peak shifts from 985 Hz to 1110 Hz when $n_{11}$ increases from 1 to 5 and from 953 Hz to 1110 Hz when $d_{11}$ increases from 0.5 mm to 1.2 mm. The decrease of impedance $Z_1$ can be deduced from equations (1) ∼ (4), and the shift of the impedance peak to the higher frequencies is mainly due to the decrease of the acoustic mass $m_{n11}$ as $n_{11}$ and $d_{11}$ increase according to the resonance frequency of LPNHR. In addition, the increase of $n_{11}$ and $d_{11}$ also lead to the decreased acoustic resistance $r_{n11}$ and the decrease of $r_{n11}$ is smaller than that of $m_{n11}$ based on the equations (7) ∼ (11), thus the bandwidth $\Delta f_1$ at the impedance of 0.5 increases by 21.1 % from 131 Hz of $n_{11}$ = 1 to 166 Hz of $n_{11}$ = 5 and by 27.1 % from 121 Hz of $d_{11}$ = 0.5 mm to 166 Hz of $d_{11}$ = 1.2 mm. When $U_0$ increases from 0 m/s to 90 m/s, the impedance peak increases by 2.203 from 0.15 to 2.353 with $n_{11}$ = 1 and $d_{11}$ = 1.2 mm, and by 0.667 from 0.141 to 0.808 with $n_{11}$ = 5 and $d_{11}$ = 1.2 mm, and by 2.591 from 0.209 to 2.8 with $n_{11}$ = 5 and $d_{11}$ = 0.5 mm. The peak frequency of LPNHR shifts by 11 Hz from 985 Hz to 974 Hz with $n_{11}$ = 1 and $d_{11}$ = 1.2 mm, and by 21 Hz from 1110 Hz to 1089 Hz with $n_{11}$ = 5 and $d_{11}$ = 1.2 mm, and by 3 Hz from 953 Hz to 950 Hz with $n_{11}$ = 5 and $d_{11}$ = 0.5 mm. The influence of the number $n_1$ and diameter $d_1$ of hole1 on the acoustic performance of LPNHR at different speeds in Fig. 4(c) is similar to that of hole11 in Fig. 4(a) and (b). In general, increasing the diameter and number of hole1 and hole11 could significantly increase the bandwidth and decrease the increment and frequency shift of the impedance peak caused by increasing main-flow velocities, but weaken the low-frequency control to a certain extent, which is more conducive to achieve near-zero suppression of aerodynamic acoustic pressure with higher main-flow velocity.

Fig. 4(d) shows the effects of the length of hole1 and hole11 on the acoustic performance of LPNHR with different main-flow velocities. When $U_0$ is 0 m/s, with the increase of $h_1 + h_{11}$ from 5 mm to 18 mm, the impedance peak shifts from 1410 Hz to

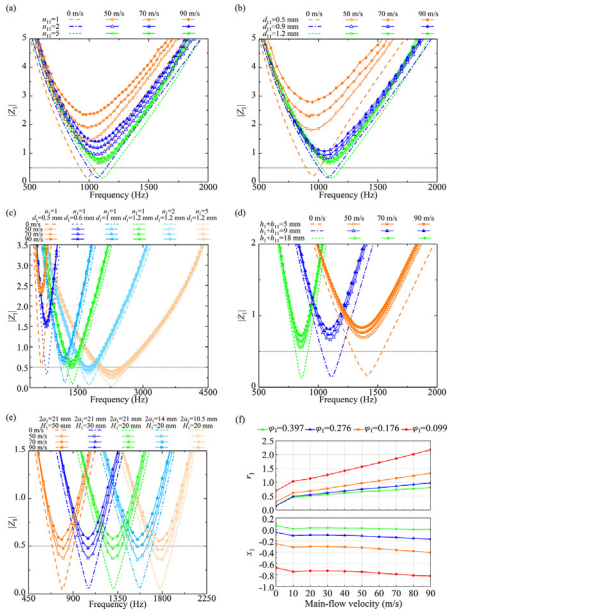


**Fig. 4.** Effects of the (a) number and (b) diameter of the hole 11, the (c) number and diameter of the hole 1, and the (d) total length of the hole 1 and hole11, and the (e) side length and height of the cavity1 on the acoustic performance of LPNHR with different main-flow velocities. (f) Simulated non-dimensional acoustic resistance and reactance of LPNHR varying with absorption area ratio and main-flow velocity at a frequency of 1100 Hz. $\varphi_1 = n_{11}\pi {d_{11}}^2/4S_1$ represents the absorption area ratio, where $S_1$ is the incident surface area.

860 Hz, and the bandwidth $\Delta f_1$ at the impedance of 0.5 decreases by 59 % from 249 Hz to 102 Hz and the magnitude of the impedance peak decreases from 0.156 to 0.114. The increased $h_1 + h_{11}$ also causes the acoustic mass $m_1$ to increase according to equations (9) ~ (11), resulting in the shift of the impedance peak to lower frequencies with unchanged cavity parameters, then the decreased acoustic resistance and increased acoustic mass make the bandwidth narrower. When $U_0$ increases from 0 m/s to 90 m/s, the impedance peak increases by 0.676 from 0.156 to 0.832 with $h_1 + h_{11}$ = 5 mm and by 0.669 from 0.141 to 0.81 with $h_1 + h_{11}$ = 9 mm, and by 0.604 from 0.114 to 0.718 with $h_1 + h_{11}$ = 18 mm. The impedance peak shifts to lower frequency by 41 Hz from 1410 Hz to 1369 Hz as $h_1 + h_{11}$ = 5 mm, and by 21 Hz from 1110 Hz to 1089 Hz as $h_1 + h_{11}$ = 9 mm, and by 3 Hz from 860 Hz to 857 Hz as $h_1 + h_{11}$ = 18 mm. Increasing the length of the hole could decrease the magnitude and frequency of the impedance peak as well as the increment and frequency shift caused by increasing main-flow velocity, thus achieving lower-frequency aerodynamic acoustic pressure suppression at higher speed, but is not conducive to broadband control.

### 3.3.2. Cavity parameters and main-flow velocities

Based on the above analysis of the neck parameters, the influences of the height $H_1$ and side length $2a_1$ of the cavity with different main-flow velocities on the acoustic performance of LPNHR are investigated in Fig. 4(e), and 2a1 = 21 mm, $2b_1$ = 1.5 mm, $l_1$ = 21.5 mm, $w_1$ = 2 mm, $n_1$ = 5, $n_{11}$ = 14, $d_1 = d_{11}$ = 1.4 mm, $h_1 = h_{11}$ = 10 mm. When $U_0$ is 0 m/s, the frequency of the impedance peak shifts from 1778 Hz to 1309 Hz as $2a_1$ increases from 10.5 mm to 21 mm and from 1309 Hz to 793 Hz as $H_1$ increases from 20 mm to 50 mm. The magnitude of the impedance peak decreases from 0.053 to 0.05 as $2a_1$ increases from 10.5 mm to 21 mm, and from 0.05 to 0.041 as $H_1$ increases from 20 mm to 50 mm. The bandwidth $\Delta f_1$ at the impedance of 0.5 decreases by 5.5 % from 271 Hz to 256 Hz as $2a_1$ increases from 10.5 mm to 21 mm and decreases by 16.0 % from 256 Hz to 215 Hz as $H_1$ increases from 20 mm to 50 mm. The shifts of the impedance peaks to lower frequencies are mainly due to the decreased equivalent stiffness of the cavity caused by the increases of $2a_1$ and $H_1$ and the decreases of impedance peaks can be deduced from equations (1) ~ (4), and the reduced acoustic resistance and weak effect of the cavity parameters on the acoustic mass make the bandwidth narrower with increased $2a_1$ and $H_1$. When $U_0$ increases from 0 m/s to 90 m/s, the magnitude of the impedance peak increases by 0.5 from 0.053 to 0.553 as $2a_1$ and $H_1$ are 10.5 mm and 20 mm, and by 0.514 from 0.05 to 0.564 as $2a_1$ and $H_1$ are 21 mm and 20 mm, and by 0.49 from 0.041 to 0.533 as $2a_1$ and $H_1$ are 21 mm and 50 mm. The impedance peak shifts by 12 Hz from 1778 Hz to 1766 Hz as $2a_1$ and $H_1$ are 10.5 mm and 20 mm, and by 9 Hz from 1309 Hz to 1300 Hz as $2a_1$ and $H_1$ are 21 mm and 20 mm, and by 7 Hz from 800 Hz to 793 Hz as $2a_1$ and $H_1$ are 21 mm and 50 mm. In general, with optimized neck parameters, the increment and frequency shift of impedance caused by increased main-flow velocity is less affected by the change of cavity parameters, increasing the side length and height of the cavity is mainly beneficial to the low-frequency control and could slightly decrease the impedance peak, thus achieving lower-frequency aerodynamic acoustic pressure suppression at higher speed.

### 3.3.3. Absorption area ratio and main-flow velocities

In Fig. 4 (f), the absolute magnitudes of both $r_1$ and $x_1$ at a frequency of $f_1$ = 1100 Hz increase to varying degrees as $U_0$ increases from 0 m/s to 90 m/s, which proves that the simulation model in this study could well describe the attenuation effect of the interaction between the acoustic field and turbulence. The values of $|r_1|$ and $|x_1|$ with the same main-flow velocity gradually increase as the absorption area ratio $\varphi_1$ decreases from 0.397 to 0.099. Moreover, the greater the absorption area ratio is, the lower the growth rate of $|r_1|$ and $|x_1|$ with increasing main-flow velocities is, that is, the better the inhibition of the weakening effect on the sound field control of LPNHR caused by increasing main-flow velocity is. The higher the main-flow velocity, more conducive it is for the LPNHR with larger absorption area ratio to achieve the near-zero suppression of the aerodynamic acoustic pressure. In total, by analyzing the effects of key parameters on the acoustic performance of LPNHR with different main-flow velocities and coordinating the close relationship between them, a low-frequency broadband LPNHR metasurface with near-zero suppression of aerodynamic acoustic pressure could be finally realized based on the multi-cell coupling.

## 4. Low-frequency broadband aerodynamic noise reduction and experimental verification

To realize the low-frequency broadband suppression of the aerodynamic noise on the 1/4-scale Ahmed body at a speed of 50 m/s, a multi-cell coupled LPNHR metasurface is constructed as shown in Fig. 5(a). Which consists of six parallel LPNHR cells with near-zero impedance at frequencies of 750 Hz (No. 1), 1100 Hz (No. 2), 1550 Hz (No. 3), 2300 Hz (No. 4), 2750 Hz (No. 5) and 3750 Hz (No. 6) at a speed of 50 m/s respectively, and each color corresponds to the same cell. Taking into account the influence of the main-flow velocities and key parameters on the acoustic performance of LPNHR and the limits of the processing accuracy of the sample, the detailed size parameters of a LPNHR basic unit are designed as shown in Table 1. Fig. 5(b) compares the mean acoustic pressure on the Ahmed upper surface when it is smooth and with LPNHR metasurface at a speed of 50 m/s within the range of 25 Hz ~ 6000 Hz. A continuous and ultra-broadband suppression of the aerodynamic acoustic pressure in a range of

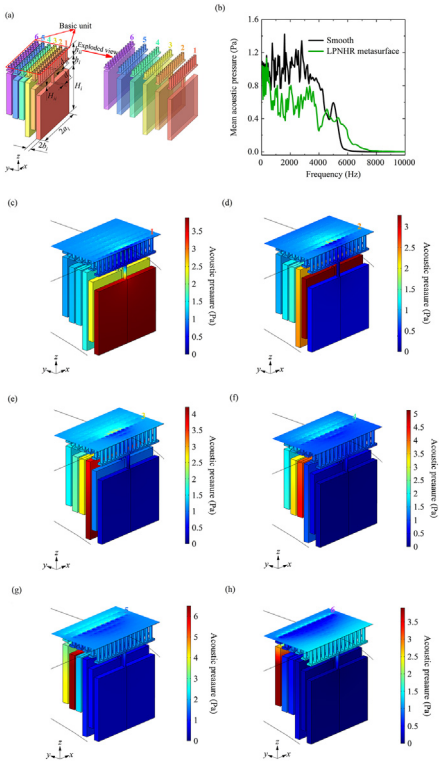


**Fig. 5.** (a) Schematic of the LPNHR basic unit composed of six parallel cells. (b) Comparison of the mean acoustic pressure on the Ahmed surface with smooth and LPNHR boundary at a speed of 50 m/s. The cloud diagram of acoustic pressure suppression at different designed frequencies of (c) 750 Hz, (d) 1100 Hz, (e) 1550 Hz, (f) 2300 Hz, (g) 2750 Hz and (h) 3750 Hz in the presence of the incident fluid flow with a velocity of 50 m/s.

550 Hz ~ 4150 Hz is realized by only six parallel LPNHR cells at a speed of 50 m/s compared with the smooth boundary. The weakening effect on the sound attenuation of the LPNHR metasurface by the flow field and the limitation of sample processing accuracy on the optimal design of the absorption area ratio make the aerodynamic acoustic pressure unable to be suppressed to zero. Ideally, when the absorption area ratio is large enough and the acoustic impedance is equal to zero, then the aerodynamic noise could be completely controlled. Fig. 5(c)-(h) show the cloud diagram of the acoustic pressure suppression at different frequencies of 750 Hz, 1100 Hz, 1550 Hz, 2300 Hz, 2750 Hz and 3750 Hz with a main-flow velocity of 50 m/s, respectively. Strong resonance occurs inside the corresponding cavities at the designed frequencies and the acoustic pressure at the LPNHR interface is suppressed nearly zero, which is in fully agreement with the theoretical analysis that the near-zero-impedance LPNHR metasurface could force the acoustic pressure at the wall approach zero, thereby suppressing the excitation of the dipole aerodynamic noise caused by flow-induced fluctuating pressure.

To verify the reliability of the above analysis results, 1/4-scale Ahmed samples corresponding to the simulation models are produced and wind tunnel test is carried out in the ducted silencer testing system at the Qingdao Branch, Institute of Acoustics, Chinese Academy of Sciences. The length of the conventional test section of this testing system is 6.9 m, and the closed loop control of the wind velocity can be realized and the designed maximum velocity can reach 60 m/s, and the average flow velocity at the test section is stabilized at 50 m/s consistent with the simulation conditions during the test. To reduce the influence of Ahmed body on the upper boundary and both sides of the test section, a 5 mm thick square-section duct is processed in the middle of the test section with the length, width and height of 2.9 m, 0.9 m and 0.9 m, which is 5 times greater than the width of the Ahmed body. The blockage ratio of the test is close to 1 % and can be ignored, and the turbulence intensity of the incoming flow is no more than 0.5 % and the axial static pressure gradient of the test section is less than 0.005 Pa/m. Fig. 6(a) shows the installation position of the Ahmed model in the wind tunnel, an 8$L$ long and 20 mm thick grounding plate extending between the two side walls in the width direction is installed 100 mm above the bottom wall of the wind tunnel to simulate the influence of the ground shear layer, which is also designed with a rounded leading edge to prevent flow separation. In Fig. 6(b), a 1/4-scale Ahmed sample with smooth surface and another with LPNHR metasurface composed of 3×3 basic unit arrays on the upper surface are made of photosensitive resin material through additive manufacturing and fixed on the surface of the grounding plate along the longitudinal centerline during the test. The length, width and height of the 1/4-scale Ahmed model is $L$,

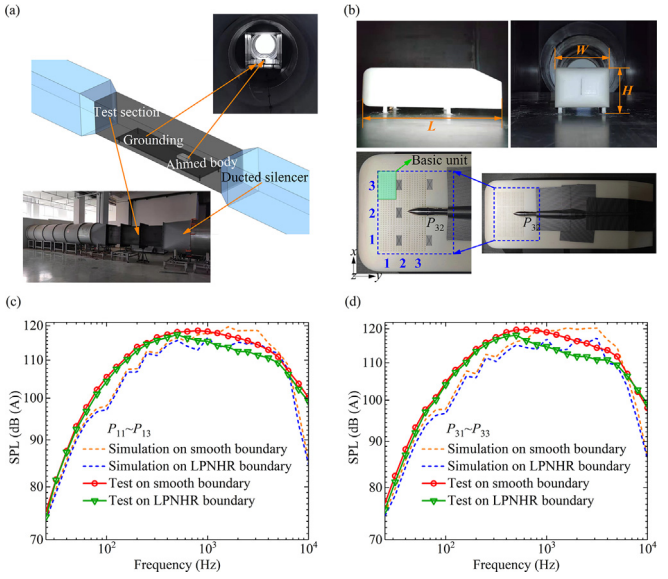


**Fig. 6.** (a) Installation of the 1/4-scale Ahmed sample in the wind tunnel. (b) The 1/4-scale Ahmed sample with LPNHR metasurface on the upper surface and arrangements of the measuring positions and microphones. Comparison of the simulated and tested values of the A-weighted one-third octave sound pressure level at (c) $P_{11}$, $P_{12}$ and $P_{13}$, and (d) $P_{31}$, $P_{32}$ and $P_{33}$ on the 1/4-scale Ahmed surface when it is smooth and with LPNHR metasurface at a speed of 50 m/s.

**Table 1**
Detailed parameters of the LPNHR cells (unit: mm).

| Unit | $2a_i$ | $2b_i$ | $l_i$ | $w_i$ | $n_i$ | $d_i$ | $h_i$ | $H_i$ | $H_{ii}$ | $n_{ii}$ | $d_{ii}$ | $h_{ii}$ |
|---|---|---|---|---|---|---|---|---|---|---|---|---|
| 1 | 21 | 1.5 | 21.5 | 2 | 1 | 0.9 | 4 | 17.5 | 0.5 | 14 | 0.9 | 4 |
| 2 | 21 | 1.5 | 21.5 | 2 | 2 | 0.9 | 3 | 16 | 0.5 | 14 | 0.9 | 3 |
| 3 | 21 | 1.5 | 21.5 | 2 | 4 | 1 | 2 | 21.2 | 0.5 | 14 | 1 | 2 |
| 4 | 21 | 1.5 | 21.5 | 2 | 6 | 1.2 | 2 | 15 | 0.5 | 14 | 1 | 2 |
| 5 | 21 | 1.5 | 21.5 | 2 | 8 | 1.3 | 2 | 14.6 | 0.5 | 14 | 1.1 | 2 |
| 6 | 21 | 1.5 | 21.5 | 2 | 11 | 1.3 | 1 | 13.9 | 0.5 | 14 | 1.3 | 1 |

$W$ and $H$, and the front face of the Ahmed sample is $2L$ from the front ends of the grounding plate, and the clearance between the bottom surface of the Ahmed body and the grounding plate is 12.5 mm. The acoustic pressure at six measuring points $P_{11}$, $P_{12}$, $P_{13}$ and $P_{31}$, $P_{32}$, $P_{33}$ are measured sequentially and three repetitive tests for each point are carried out to avoid random errors in data collection. Siemens SCM202 multi-channel data acquisition instrument and the GRAS 1/4-inch microphone and amplifier are used during the test. A nose cone made by imitation of Danish B&K is installed on the microphone to reduce the self-noise tones, and the basic characteristics of this imitated nose cone are verified to be comparable to B&K nose cone through performance test [39]. Fig. 6(c) and (d) show the A-weighted one-third octave sound pressure level on the Ahmed body surface through simulation and wind tunnel tests at a speed of 50 m/s. The tested sound energy on the Ahmed upper surface is mainly low-mid frequency in a large broadband, and the noise levels within 100 Hz - 6000 Hz are basically above 100 dB (A) and decrease rapidly when the frequency exceeds 6000 Hz. The tested results below 800 Hz are greater than the simulated values, the larger tested value is mainly due to the low-frequency noise sources resulted from the structural vibration of the air duct and the grounding plate, and the errors between the simulation and test gradually decrease since the reduced low-frequency noise source as the frequency increases, which also confirms the process that the influence of low-frequency structural vibrations is gradually weakened with the increasing frequency. When the frequency exceeds 800 Hz, the simulation gradully becomes larger than the test value. This can be attributed to the fact that the ground is set as a solid wall in the simulation so that the received noise can be fully reflected without attenuation, while the floor absorbs a large amount of noise in the test. Despite the differences between the simulation and testing, the average error between the two curves is less than 3 % over the whole frequency range and the trend of the tested aerodynamic noise is basically consistent with the simulation results. Most importantly, both the simulation and test achieve effective control of aerodynamic noise in the designed frequency range at a speed of 50 m/s. Finally, average reductions of sound pressure levels by 2.75 dB (A) and 3.71 dB (A) at $P_{11} \sim P_{13}$ and $P_{31} \sim P_{33}$ on the LPNHR boundary in the range of 550 Hz - 4150 Hz are measured compared with the smooth boundary, which well verifies the reliability of the flow-acoustic coupling simulation and wind tunnel test in this study and the effectiveness of LPNHR metasurface design for low-frequency broadband aerodynamic noise reduction.

## 5. Conclusions

The near-zero aerodynamic acoustic pressure suppression mechanism of an ultra-thin low-frequency and broadband LPNHR metasurface with a basic unit composed of six parallel cells is presented, and an average sound pressure level reduction of 3.71 dB (A) in the range of 550 Hz - 4150 Hz on the 1/4-scale Ahmed surface at a speed of 50 m/s is experimentally verified based on the larger bandwidth of LPNHR, near-zero suppression of low-frequency aerodynamic acoustic pressure and coupling multi-cavity resonance. This mechanism can be implemented through changing the single neck of HR into a lotus-pods multi-layer-hole neck and keeping the number and equivalent diameter of holes in the upper layer greater than that in lower layer, so that the bandwidth of LPNHR is wider than that of HR due to the decreased acoustic mass. Under incident fluid flow, the near-zero suppression of low-frequency aerodynamic pressure with LPNHR can be mainly attributed to the formation of the greater counterclockwise pressure difference in each hole generating stronger multi-vortexes and larger multi-vortex areas, which result in the increased average flow velocity at the neck interface and then the decreased impedance. Moreover, the stronger multi-vortexes enhance the flow from the external flow field into the LPNHR neck, causing further reduction of the impedance and increase in effective length of the neck and acoustic mass, the shift of the sound attenuation to higher frequencies affected by fluid flow is suppressed and turned to lower frequencies. When the impedance approaches zero, the incident and scattered acoustic pressure match in phase and the acoustic pressure fluctuation at the wall will be fundamentally suppressed, which is the physical mechanism of LPNHR to achieve near-zero suppression of low-frequency aerodynamic acoustic pressure. Furthermore, by adjusting the neck parameters, cavity parameters and absorption area ratio, the near-zero suppression of lower-frequency and larger-bandwidth aerodynamic acoustic pressure at higher speed could be achieved. This study sheds light on the effectively control of the low-frequency aerodynamic noise with acoustic metamaterials, showing great potential in engineering applications.

## CRediT authorship contribution statement

**Min Li:** Conceptualization, Methodology, Software, Validation, Investigation, Formal analysis, Resources, Writing – original draft, Writing – review & editing. **Jiu Hui Wu:** Conceptualization, Investigation, Resources, Writing – review & editing, Supervision, Project administration, Funding acquisition. **Bo Bo Wu:** Validation, Investigation, Formal analysis, Resources, Writing – review & editing. **Chong Rui Liu:** Software, Validation, Writing – review & editing. **Fu Yin Ma:** Validation, Formal analysis, Writing-review & editing. **Xiao Yang Yuan:** Investigation, Supervision, Project administration. **Yang Bin Sun:** Supervision, Project administration, Funding acquisition.

## Data availability

No data was used for the research described in the article.

## Declaration of Competing Interest

The authors declare that they have no known competing financial interests or personal relationships that could have appeared to influence the work reported in this paper.

## Acknowledgements

This work was supported by the National Natural Science Foundation of China (NSFC) under Grant No.51705395 and Foundation from National Key Laboratory on Ship Vibration and Noise, China Ship Development and Design Center under Grant No. JCKY2020207CI01.

## Data availability statement

The data that support the findings of this study are available from the corresponding author upon reasonable request.

## References

[1] Talotte C. Aerodynamic noise: A critical survey. J Sound Vibr 2000;231(3):549–62.
[2] Sassa T, Sato T, Yatsui S. Numerical analysis of aerodynamic noise radiation from a high-speed train surface. J Sound Vibr 2001;247(3):407–16.
[3] Tan XM, Liu HF, Yang ZG, Zhang J, Wang ZG, Wu YW. Characteristics and mechanism analysis of aerodynamic noise dources for high-speed train in tunnel. Complexity 2018;5858415.

[4] Dai WQ, Zheng X, Hao ZY, Qiu Y, Li H, Luo L. Aerodynamic noise radiating from the inter-coach windshield region of a high-speed train. J Low Freq Noise Vib Act Control 2018;37(3):590–610.
[5] Schetz J. Aerodynamics of high-speed trains. Annu Rev Fluid Mech 2001;33:371–414.
[6] King WF. Effect of motion on acoustic dipole models for aerodynamic noise prediction. Phys Lett A 1977;62(4):282–4.
[7] Sun ZX, Guo DL, Yao SB, Yang GW, Li MG. Identification and suppression of noise sources around high speed trains. Eng Appl Comp Fluid Mech 2013;7 (1):131–43.
[8] Yang YZ, Jia H, Lu WJ, Sun ZY, Yang J. Impedance-matching acoustic bend composed of perforated plates and side pipes. J Appl Phys 2017;122 (5):054502.
[9] Liu CK, Luo J, Lai Y. Acoustic metamaterials with broadband and wide-angle impedance matching. Phys Rev Mater 2018;2(4):45201.
[10] Ding YH, Statharas EC, Yao K, Hong MH. A broadband acoustic metamaterial with impedance matching layer of gradient index. Appl Phys Lett 2017;110 (24):241903.
[11] Al Jahdali R, Wu Y. High transmission acoustic focusing by impedance-matched acoustic meta-surfaces. Appl Phys Lett 2016;108(3):031902.
[12] Bai L, Dong HY, Song GY, Cheng Q, Huang B, Jiang WX, et al. Impedance-matching wavefront-transformation lens based on acoustic metamaterials. Adv Mater Technol 2018;3(11):1800064.
[13] Kozlov VF, Fedorov AV, Malmuth ND. Acoustic properties of rarefied gases inside pores of simple geometries. J Acoust Soc Am 2005;117(6):3402–12.
[14] Bres GA, Colonius T, Fedorov AV. Acoustic properties of porous coatings for hypersonic boundary-layer control. AIAA J 2010;48(2):267–74.
[15] Bres GA, Inkman M, Colonius T, Fedorov AV. Second-mode attenuation and cancellation by porous coatings in a high-speed boundary layer. J Fluid Mech 2013;726:312–37.
[16] Radavich PM, Selamet A, Novak JM. A computational approach for flow-acoustic coupling in closed side branches. J Acoust Soc Am 2001;109(4):1343–53.
[17] Howard CQ, Craig RA. Noise reduction using a quarter wave tube with different orifice geometries. Appl Acoust 2014;76:180–6.
[18] Phillips B. Effects of high-wave amplitude and mean flow on a Helmholtz esonator. NASA Technical Memorandum 1968; NASA TM X-1582.
[19] Hersh A, Walker B. Effect of grazing flow on the acoustic impedance of Helmholtz resonators consisting of single and clustered rifices. AlAA 11th fluid and plasma dynamics conference. 1978; NASA CR-3177.
[20] Meyer E, Mechel F, Kurtze G. Experiments on the influence of flow on sound attenuation in absorbing ducts. J Acoust Soc Am 1958;30(3):165–74.
[21] Anderson JS. The effect of an air flow on a single side branch helmholtz resonator in a circular duct. J Sound Vibr 1977;52(3):423–31.
[22] Marx D, Auregan Y, Bailliet H, Valiere JC. PIV and LDV evidence of hydrodynamic instability over a liner in a duct with flow. J Sound Vibr 2010;329(18):3798–812.
[23] Zhao R, Liu T, Wen CY, Zhu J, Cheng L. Impedance-near-zero acoustic metasurface for hypersonic boundary-layer flow stabilization. Phys Rev Appl 2019;11(4):044015.
[24] Langfeldt F, Hoppen H, Gleine W. Broadband low-frequency sound transmission loss improvement of double walls with Helmholtz resonators. J Sound Vibr 2020;476:115309.
[25] Mi YZ, Yu X. Attenuation of low-frequency sound in u-shaped duct with membrane coupled acoustic resonator: Modeling and analysis. J Sound Vibr 2020;489:115679.
[26] Klaus J, Bork I, Graf M, Ostermeyer GP. On the adjustment of Helmholtz resonators. Appl Acoust 2014;77:37–41.
[27] Yang M, Sheng P. Sound absorption structures: from porous media to acoustic metamaterials. Ann Rev Mater Res 2017;47:83–114.
[28] Jiang PT, Jiang TX, He QB. Origami-based adjustable sound-absorbing metamaterial. Smart Mater Struct 2021;30(5):057002.
[29] Wang YH, Zhang CC, Ren LQ, Ichchou M, Galland MA, Bareille O. Sound absorption of a new bionic multi-layer absorber. Compos Struct 2014;108:400–8.
[30] Li M, Wu JH, Yuan XY. Metasurface zero-impedance matching mechanism for aerodynamic noise reduction. J Sound Vibr 2022; 536:117147.
[31] Camussi R, Guj G, Ragni A. Wall pressure fluctuations induced by turbulent boundary layers over surface discontinuities. J Sound Vibr 2006;294(1-2):177- 204.
[32] Li M, Wu JH, Yuan XY. Broadband suppression of aerodynamic pressure on the high-speed bluff body surface with periodic square-cavity acoustic metasurface. AIP Adv 2021;11(10):105004.
[33] Stinson MR. The propagation of plane sound-waves in narrow and wide circular tubes, and generalization to uniform tubes of arbitrary cross-sectional shape. J Acoust Soc Am 1991;89(2):550-558.
[34] Li M, Wu JH, Yuan XY. Wall suction & slip effect of spherical-grooved bionic metasurface for controlling the aerodynamic noise. Appl Acoust 2021;171:107537.
[35] Pollack ML. Acoustic inertial end correction. J Sound Vibr 1979;67(4):558-561.
[36] Elder SA. Active end correction of pipes and resonators. J Acoust Soc Am 1967;41(6):1609-&.
[37] Selamet E, Selamet A, Iqbal A, Kim H. Effect of flow on Helmholtz resonator acoustics: a three-dimensional computational study vs. experiments. SAE Tech Pap 2011;2011-01-1521.
[38] Ni HG, Chen X. Discussion on hydraulic properties of plane vortex with standing center. J Hydraul Eng 1998;29(11):50–56.
[39] Fields R, Jin T, Soderman P. An experimental investigation of flow-induced tones of the Brueel and Kjaer in-flow microphone. 3rd AIAA/CEAS Aeroacoustics Conference 1997;AIAA-97-1674-CP.